Available online at www.sciencedirect.com
SCIENCE DIRECT®
Journal of Magnetic Resonance 177 (2005) 9–21
JMR Journal of Magnetic Resonance
www.elsevier.com/locate/jmr

# Multiple-quantum vector field imaging by magnetic resonance

Louis-S. Bouchard *, Warren S. Warren *

*Department of Chemistry, Princeton University, Princeton, NJ 08544, USA*

Received 19 April 2005; revised 25 June 2005
Available online 8 August 2005

**Abstract**

We introduce a method for non-invasively mapping fiber orientation in materials and biological tissues using intermolecular multiple-quantum coherences. The nuclear magnetic dipole field of water molecules is configured by a CRAZED sequence to encode spatial distributions of material heterogeneities. At any given point **r** in space, we obtain the spherical coordinates of fiber orientation $(\theta,\phi)$ with respect to the external field by comparing three signals $\|G_X\|$, $\|G_Y\|$, and $\|G_Z\|$ (modulus), acquired with linear gradients applied along the $X$, $Y$, and $Z$ axes, respectively. For homogeneous isotropic materials, a subtraction $\|G_Z\| - \|G_X\| - \|G_Y\|$ gives zero. With anisotropic materials, we find an empirical relationship relating $\|G_Z\| - \|G_X\| - \|G_Y\|/(\|G_X\| + \|G_Y\| + \|G_Z\|)$ to the polar angle $\theta$, while $\|G_X\| - \|G_Y\|/(\|G_X\| + \|G_Y\| + \|G_Z\|)$ is related to the azimuthal angle $\phi$. Experiments in structured media confirm the structural sensitivity. This technique can probe length scales not accessible by conventional MRI and diffusion tensor imaging.


*Keywords:* Distant dipolar field; Intermolecular multiple-quantum coherences; Porous materials; Material anisotropy; Microstructure; Vector mapping

## 1. Introduction

Magnetic resonance imaging (MRI) generally performs poorly in terms of spatial resolution compared to other modalities such as electron microscopy, light microscopy, particle, and X-ray scattering. Of particular concern, the resolution of clinical MRI systems is limited to voxels on the millimeter scale. Pulsed-field gradient techniques extend the realm of NMR microscopy by probing diffusion lengths of a few micrometers. For example, diffusion tensor imaging (DT-MRI) [1] probes tissue structure on the micrometer scale at any position **r** in three-dimensional space. Its potential for clinical applications (stroke, trauma, schizophrenia, and multiple sclerosis) and tracking bundles of nerve fibers in white matter to map neuronal connectivity [2] has been proposed. Despite this progress, intermediate regimes, where the length scale ranges from hundreds of micrometers to millimeters, are still generally difficult or impossible to access.

Many examples of porous materials exist in the materials sciences which would benefit from methods of structure assessment at the intermediate length scales. Likewise, the assessment of tissue structure in vivo in the search for possible correlations with the state of disease are of interest. Examples include bone loss, which occurs in postmenopausal osteoporosis or extended exposure to microgravity, where architectural changes in the bone structure, such as the degree of structural anisotropy and topology, are associated with the progress of disease and monitoring the effects and progress of novel therapies. A related problem is the assessment of solid tumor structure, for which networks of blood vessels proliferate rapidly. NMR is not the modality of choice for resolving the structures, and in bone, diffusion-based methods are not an option because the pores are too large. Given the important role of MRI

* Corresponding authors. Fax: +1 510 486 5744 (L.-S. Bouchard).
*E-mail addresses:* LSBouchard@waugh.cchem.berkeley.edu (L.-S. Bouchard), warren.warren@duke.edu (W.S. Warren).

1090-7807/$ - see front matter © 2005 Elsevier Inc. All rights reserved.
doi:10.1016/j.jmr.2005.06.019

in diagnostic biomedicine, improved methods to probe intermediate length scales would be desirable.

Intermolecular multiple-quantum coherences (iMQC) which arise from long range nuclear dipole–dipole couplings in solution are attractive because of their ability to encode material geometry over intermediate length scales, whether it is contained inside an imaging voxel or buried in the total signal. We have recently demonstrated [3] the ability of the NMR CRAZED experiment [4,5] to reconstitute the geometry of a volume element (voxel) by encoding of the solid phase using the dipolar field of the solution phase. Thus, NMR microscopy and sub-voxel resolution in MRI is possible with the dipolar field. Because the signal can be averaged over volumes larger than the structure size, there is no penalty in sensitivity. (By this, we mean that one may circumvent the loss of SNR in conventional MRI that is associated with the choice of smaller voxels.) In this article, we present a simplified method which does not require reconstruction and can readily detect structural anisotropy in a material with the use of two simple empirical relations.

The idea of using the distant dipolar field to extract microstructural parameters in a material is not new; it has been introduced over a decade ago [6,4,7–9]. The first experimental demonstration of intermolecular dipolar couplings between spins located in isolated regions of space is due to Warren [4]. Subsequent work by the group of Bowtell [10,9,11,12] provided in-depth theoretical and experimental characterizations of the behavior of CRAZED signals in structured samples. In particular, Robyr and Bowtell [12] proved that spatial autocorrelation functions of the void phase could be extracted by Fourier transformation of the CRAZED signal from bulk measurements (i.e., without spatial selectivity) as function of wave vector $\mathbf{k}$. Novel image contrast in vivo was first demonstrated by Warren [5]. It was later shown experimentally and via numerical calculations that iMQC image contrast is sensitive to local magnetization density differences in structured materials despite image voxel sizes smaller to the dipolar correlation distance [13]. The sensitivity of iMQCs to local resonance frequency differences also suggests applications to tumor detection [5,14], functional MRI [15–17] and to characterizing the microscopic structure of trabecular bone [18,19]. In the latter case, parameters of interest which can be extracted include mean trabecular spacing (Chin et al. [19]) and structural anisotropy (Bouchard et al. [18]). Brown et al.[20,21] used the method to extract an average bubble size measurement in oil–water emulsions.

In the general vector mapping problem, one seeks integral curves $\gamma:(a,b)\to M$ of $\mathcal{X}$, where $M$ is a region of space. These "flow lines" are solutions to the equation $\gamma\prime(t)=\mathcal{X}(\gamma(t))$. The vector field $\mathcal{X}$ is mapped as a function of $\mathbf{r}$. In DT-MRI, $\mathcal{X}(\mathbf{r})$ is tangent to the principal eigenvector of the diffusion tensor at $\mathbf{r}$. In this article, the vector field at $\mathbf{r}$ is given as spherical coordinates on the unit sphere $\mathcal{X}(\mathbf{r})=\mathcal{X}_\theta(\mathbf{r})\frac{\partial}{\partial\theta}|_{\mathbf{r}}+\mathcal{X}_\phi(\mathbf{r})\frac{\partial}{\partial\phi}|_{\mathbf{r}}$, where $\mathcal{X}_\theta(\mathbf{r})$ and $\mathcal{X}_\phi(\mathbf{r})$ are the components of the vector field. For a fixed $\mathbf{r}$, we construct maps $g:\theta\to C(\|G_Z\|-\|G_X\|-\|G_Y\|)$ and $h:\phi\to C(\|G_X\|-\|G_Y\|)$, where $\|G_X\|$, $\|G_Y\|$, and $\|G_Z\|$ are the absolute values of the CRAZED signal within a voxel $V$ centered at $\mathbf{r}$ measured with correlation gradients along $x$, $y$, and $z$, respectively, containing fiber(s) with orientation $(\theta,\phi)$. $C$ is a normalization factor given by $1/C=\|G_Z\|+\|G_X\|+\|G_Y\|$. As shown later, the components of the vector field are obtained from the inverse maps $\mathcal{X}_\theta=g^{-1}$ and $\mathcal{X}_\phi=h^{-1}$.

We show that structural anisotropy can be readily measured in materials, even when the structures are too small to be resolved individually by conventional imaging. Ex vivo results in the rat brain (Fig. 11) reveal that subtraction signals in the cerebral cortex can be measured in animal tissue, suggesting possible applications in vivo.

### 1.1. CRAZED sequence

In this study, we use the double-quantum ($n=2$) CRAZED sequence [4,5], consisting of preparation and detection periods. A pair of correlation gradient pulses is applied in 2:1 ratio. In a quantum mechanical framework [22], this filter passes signals originating from coherent phase evolutions at approximately twice the Larmor frequency during the evolution period (9). These "second harmonics" refocus to produce signals that are proportional to the magnetic dipole field.

BIR-4 adiabatic pulses were used for excitation, phase modulated slice-selective hyperbolic secant pulses for slice selection (slices were 4 mm thick), followed by acquisition of a single line in $k$-space using phase and frequency encoding. The preparation period is the sequence

$$\mathcal{R}(\beta_1)-\frac{\tau}{2}-\mathcal{R}(2\pi)-\frac{\tau}{2}-GT-\mathcal{R}(\beta_2)-2GT-\tau-\mathcal{R}(2\pi)-\tau,$$

where $\mathcal{R}(\theta)$ denotes a rotation (RF pulse) by angle $\theta$. The flip angles are $\beta_1=\pi/2$ and $\beta_2=2\pi/3$. $2GT$ and $GT$ are the correlation gradients in ratio 2:1. (For clarity, RF and gradient pulses have zero duration in the above timing sequence; delays shown are from one RF pulse to the next.) This preparation is followed by the detection sequence:

$$\frac{TE}{4}-\mathcal{R}(\pi)-\frac{TE}{2}-\mathcal{R}(\pi)-\frac{TE}{4}-\text{acquire}.$$

This sequence differs slightly from the original CRAZED [5] by allowing the switching to MOD-CRAZED mode [23] by changing the dummy $2\pi$ pulses to refocusing $\pi$ pulses. In this study, we consider only

CRAZED measurements. Magic angle crusher pulses conclude the preparation/acquisition by nulling the average magnetization prior to the next acquisition [5]. Unless otherwise specified, the parameters were: 3 cm field of view, $128 \times 128$ matrix, TR=3 s, and TEeff = 90 ms (TEeff is the effective echo time, defined for the $n = 2$ CRAZED sequence as TE + $2\tau$). Two values of $\tau$ were used, 6 and 36 ms, with similar results, therefore only the $\tau = 36$ ms data are shown. In heterogeneous media, longer values of $\tau$ in a CRAZED experiment amplify the effects of local resonance frequency offsets [5].

### 1.2. NMR image contrast in celery

Celery has vascular tissues that provide a sufficiently heterogeneous structure in terms of NMR properties to demonstrate the technique of vector imaging. The vascular bundles (VB) are organized into collateral xylem and phloem strands (Fig. 1, inset). The VB and collenchyma (Fig. 1) form a highly anisotropic vascular network along the direction of the celery with relatively uniform proton density. However, for RF excitations repeated at time intervals TR, the magnetization establishes an equilibrium which depends on the proton density and recovery time $T_1$; lower relaxation times $T_1$ combined with short repetition times TR result in stronger steady-state signal intensity, as seen in Fig. 2.

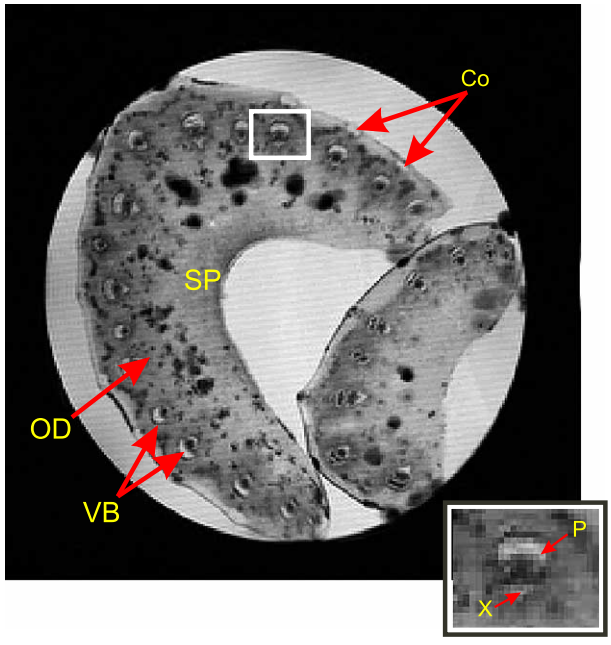


Fig. 1. Magnetic resonance image of celery (spin echo acquisition with TE = 122 ms, TR = 2 s, $256 \times 256$, 3 cm field of view, 4 mm slice thickness) showing vascular tissues of two celery sticks. Co, collenchyma; SP, storage parenchyma; VB, vascular bundle; OD, oil ducts. Inset: enlarged view of vascular bundle depicting the xylem (X), and phloem (P) tissues.

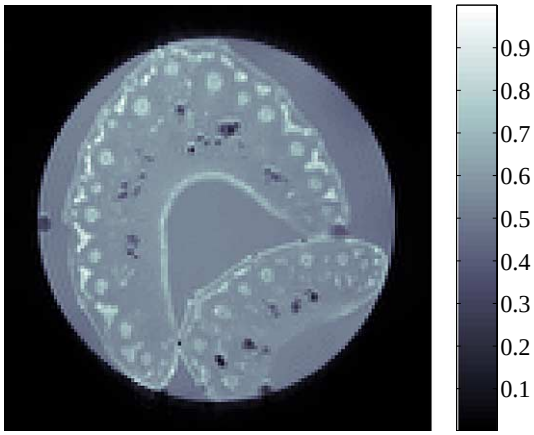


Fig. 2. $T_1$-weighted steady-state longitudinal magnetization ($M_{eq}$) map acquired with TR = 3 s illustrate regions of larger (60%) longitudinal equilibrium magnetization in the vascular bundles, collenchyma and neighboring regions. The vascular bundles and collenchyma vessels constitute highly anisotropic structures pointed along the direction of the celery (out of plane).

The higher equilibrium longitudinal magnetization (60% higher than the surrounding background parenchyma) is a heterogeneous structure that modulates the dipolar field. Measurements of $T_1$ and proton density confirm that the partial suppression of the water signal comes from its longer $T_1$ value.

## 2. Results

### 2.1. Empirical relationships of vector orientation

In this section, we derive two important empirical relationships which relate the fiber orientation to the

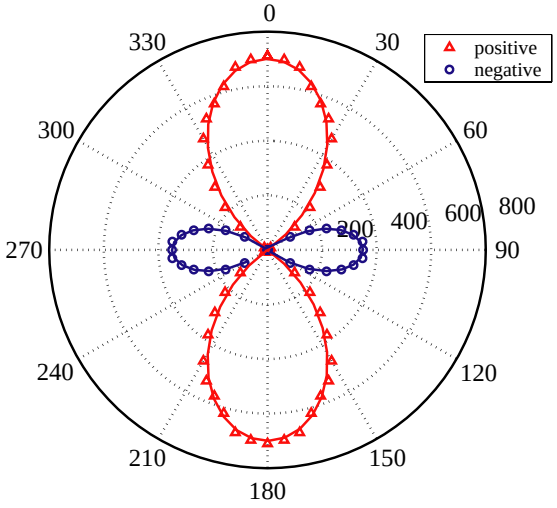


Fig. 3. Rotation of the correlation gradient in the $yz$ plane from $\theta = 0°$ (along $z$) to $\theta = 90°$ (along $y$) for a sphere. The symbols indicate the real part of the bulk complex-valued signal while the line is a plot of $const \cdot (3\cos^2\theta - 1)$.

Fig. 4. (A–C) Plots of calculated bulk CRAZED signals with $x$, $y$, and $z$ gradients and (D–F) the corresponding subtractions $\|G_Z\| - \|G_X\| - \|G_Y\|$ for fibers rotated from the $z$ axis ($\theta = 0°$) towards the $y$ axis ($\theta = 90°$). (A and D) For a single fiber (radius 30 pts, length 80 pts, $d_c = 12$ pts) with magnetization density 1.0 inside and 0 outside. (B and E) Array of four fibers (radius 10, length 80, $d_c = 4$ pts). (C and F) Same four fibers but for $d_c = 12$ pts. In all cases (D–F) an angular dependence similar to $3\cos^2\theta - 1$ is observed, making it possible to determine the spherical polar angle $\theta$ of the fiber orientation. (For clarity, only the first quadrant is shown. All plots have the full rotational symmetry as in Fig. 3.)

Fig. 5. (A–C) Calculated bulk CRAZED signals with $x$, $y$, and $z$ gradients for the square array of four fibers (length = 70 pts, radius = 10 pts) parallel to the $xy$ plane, and rotated from the $y$ axis ($\phi = 0°$) towards the $x$ axis ($\phi = 90°$). (For clarity, only the first quadrant is shown. All plots have the full rotational symmetry as in Fig. 3.)

CRAZED NMR signal. This establishes the theoretical grounds for our vector imaging methodology. We calculate the CRAZED signal using the simple model where the signal is proportional to the dipolar field (linear approximation) [3,24,25]. The signal of a CRAZED sequence at short evolution times is the complex quantity $S_x + iS_y$. For numerical evaluations of the CRAZED signal we use the discrete form, which, for the $i$th Cartesian component of the total magnetization vector $\vec{S}(\mathbf{k})$ is given by $S_i = \sum_{\mathbf{r}_l} M_j(\mathbf{r}_l)B_k(\mathbf{r}_l) - M_k(\mathbf{r}_l)B_j(\mathbf{r}_l)$, where $i,j,k$ refer to the vector components $x,y,z$ and cyclic permutations and the sum includes all discrete grid elements covering the sample. (See Bouchard and Warren [3] for details.) $\vec{M}(\mathbf{r})$ is the magnetization at position $\mathbf{r}$ following the CRAZED preparation; it is modulated by the correlation gradient according to the wave vector $\mathbf{k} = \gamma T\mathbf{G}$, which determines the correlation distance $d_c = \lambda/2 = \pi/|\mathbf{k}|$. It is known that for such a sequence, the bulk of the signal at $\mathbf{r}$ originates from dipolar couplings involving spins located at a distance of order $d_c$ [4,22]. $\vec{B}(\mathbf{r})$ is the dipolar field at $\mathbf{r}$ exerting a torque on the magnetization vector $\vec{M}$. Since it depends on the field $\vec{M}$, $\vec{B}$ also depends on $\mathbf{k}$. We calculate the Fourier transformation $\vec{M}(\mathbf{r}) \to \tilde{M}(\mathbf{k})$ and use Deville's [26] expression $\tilde{B}(\mathbf{k}) = (4\pi/6)[3\tilde{M}_z(\mathbf{k})\hat{\mathbf{z}} - \tilde{M}(\mathbf{k})] \quad (1 - 3(\hat{\mathbf{k}} \cdot \hat{\mathbf{z}})^2)$, followed by inverse Fourier transformation $\tilde{B}(\mathbf{k}) \to \vec{B}(\mathbf{r})$. Each calculation of $\vec{S}(\mathbf{k})$ is repeated four times on a discrete cubic grid of $128^3$ evenly spaced points with cycling of the first RF pulse phase $0, \pi, \pi/2, 3\pi/2$ and receiver phase $0, 0, \pi, \pi$. The magnetization distribution $\vec{M}(\mathbf{r})$ for a given sample geometry following the CRAZED sequence is calculated by application of rotation matrices for infinitely short RF and gradient pulses, while neglecting non-linear evolution during the preparation.

A sample calculation is shown in Fig. 3, which is a polar plot of the CRAZED signal intensity as function of correlation gradient direction, for a sphere with equilibrium magnetization density 1.0 and radius 34 pts discretized on a $128^3$ grid, correlation distance $d_c = 22$ pts, and zero magnetization in the surrounding space. The calculation correlates to the solid line, which is the scaled function $\text{const} \cdot (3\cos^2\theta - 1)$, known to describe the strength of the truncated dipolar field for a magnetized sphere with sinusoidally modulated magnetization [22]. $\theta$ is the angle of the magnetic field gradient with respect to the positive $z$ axis. As the gradient is rotated, $\mathbf{k}$ remains in the $yz$ plane.

For this isotropic object, a subtraction $\|G_Z\| - \|G_X\| - \|G_Y\|$ gives zero, where $\|G_Z\|$ is the magnitude of the signal for an applied $z$ gradient, and so on. This is because $\|G_X\|$ and $\|G_Y\|$ are both 1/2 the magnitude of $\|G_Z\|$. A more interesting question is whether $\|G_Z\| - \|G_X\| - \|G_Y\|$ is nonzero in samples which are not isotropic, and if the sample orientation alters the value of $\|G_Z\| - \|G_X\| - \|G_Y\|$. By symmetry of the dipolar field, the signal in Fig. 3 is, of course, independent of a rotation of the azimuthal angle $\phi$ of the gradient.

A reasonable approximation for the VB or collenchyma vessels is a fiber or cylinder whose equilibrium magnetization density differs from the surrounding material. It may be shown (see Appendix A) that, to calculate changes in signal intensity, it is not necessary to include the embedding material; for small enough perturbations[1], it is sufficient to calculate the effects on the isolated perturbation. In light of this, we model an embedded heterogeneity which consists of a shift in magnetization density from the surrounding material as an isolated perturbation without the surrounding material.

Figs. 4A–C are plots of the calculated CRAZED signal for $x$, $y$, and $z$ gradients (magnitude of the complex number $S_x + iS_y$ as calculated for $\hat{\mathbf{k}} = \hat{\mathbf{x}}, \hat{\mathbf{y}}$, and $\hat{\mathbf{z}}$) for fibers rotated about the $x$ axis by an angle $\theta$ ($\theta = 0$ corresponds to $\hat{\mathbf{z}}$; $\theta = \pi/2$ to $\hat{\mathbf{y}}$). $\phi$ is held constant at $\phi = 0$ throughout the rotation, where $\phi = 0$ points along the $y$ axis. The fibers have $M_{\text{eq}} = 1.0$ while the surrounding medium is empty, i.e., $M_{\text{eq}} = 0.0$. Fig. 4A is for a cylindrical fiber of length 80 grid pts and radius 30 pts, at the center of the $128^3$ grid; Fig. 4B is for a square array of four parallel fibers, length 80 pts and radius 10 pts, with cylinder centers spaced 26 pts apart.

In the case of Figs. 4A and B the correlation distance $d_c$ is 0.4 times the cylinder radius ($d_c$ is 12 pts for Fig. 4A and 4 pts for Fig. 4B). In both cases, the signal dependence on $\theta$ is similar and shows a 2:1 ratio of amplitudes for the $z$ gradient compared to a $x$ or $y$ gradient. The amplitudes of $x$, $y$, and $z$ gradient curves in Fig. 4A

[1] "Small" refers to the relative volume and magnetization density difference.

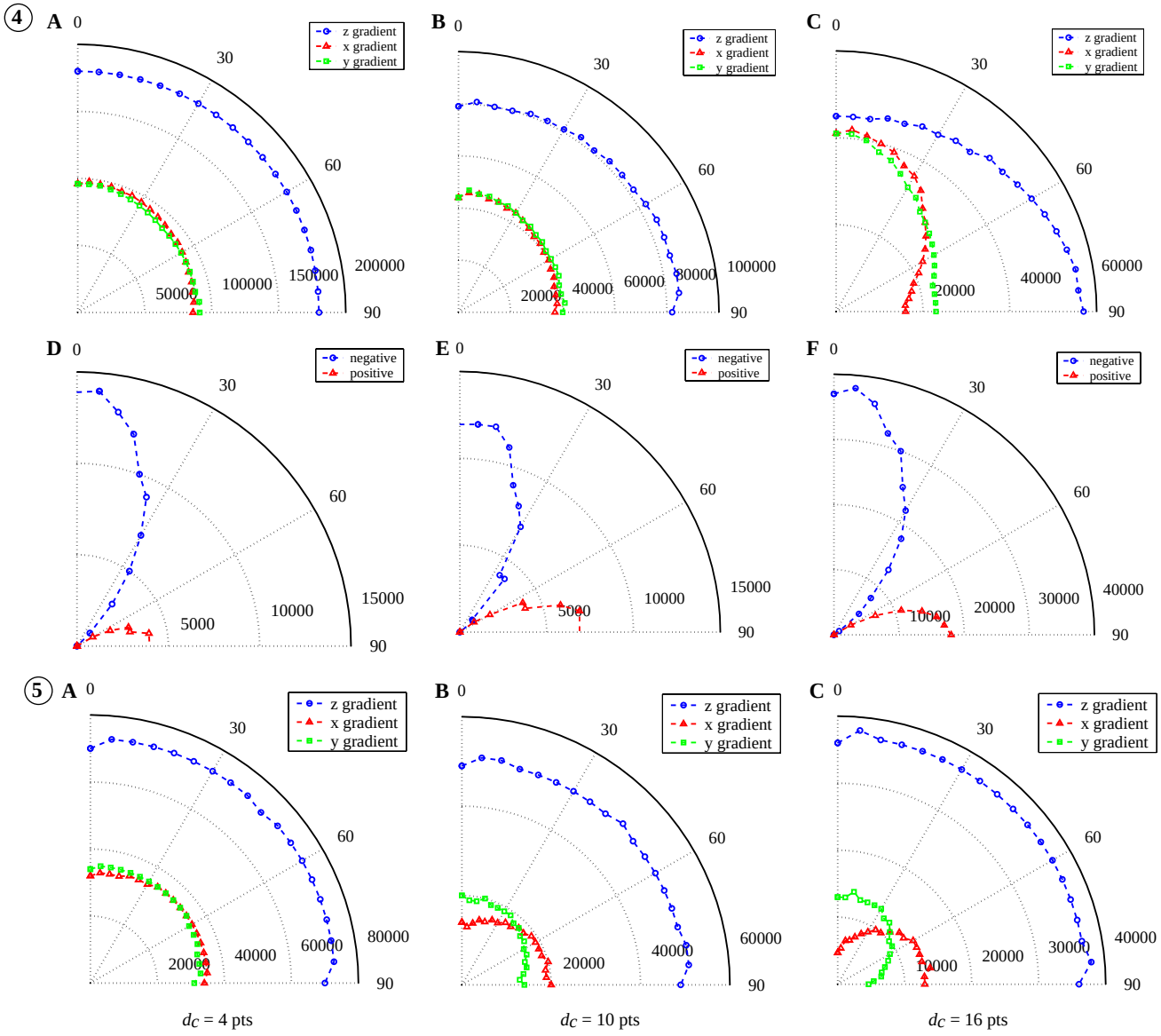


are roughly twice those of Fig. 4B because the volume fraction (*v.f.*) of the single cylinder (*v.f.* = 0.11) is nearly twice that of the array of four cylinders (*v.f.* = 0.05).

Figs. 4D and E are the corresponding subtractions of $x$ and $y$ curves from the $z$ curve, which we symbolically denote $\mathcal{S}$ (where $\mathcal{S} = \|G_Z\| - \|G_Y\| - \|G_X\|$), plotted as function of $\theta$, the rotation angle of the fibers. While $\|G_Z\|$, $\|G_Y\|$, and $\|G_X\|$ are magnitudes, their subtraction $\mathcal{S}$ can be positive or negative, as indicated by the different symbols. We note the striking similarity of the angular dependence to the function $3\cos^2\theta - 1$, including the sign dependence. That is, there are negative lobes centered at the poles ($\theta = 0$) and positive lobes near the equatorial plane ($\theta = \pi/2$), and $\mathcal{S}$ converges to zero when approaching the magic angle.

This suggests empirically the existence of a $2-1$ mapping between $\theta \in [0, \pi)$ and $\mathcal{S}$: given a measurement of the number $\mathcal{S}$ at position $\mathbf{r}$, its sign indicates whether

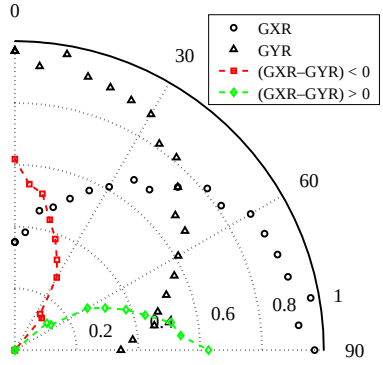


Fig. 6. Plots of *GXR* and *GYR* ratios for the four 4 fibers (length = 70 pts, radius = 10 pts) rotated in the $xy$ plane. Their difference $GXR - GYR$ permits the determination of the azimuthal angle $\phi$. 0° corresponds to the fibers pointed along $y$, and 90°, along $x$. An angular dependence of the type $2\cos^2\phi - 1$ is observed, making it possible to determine the spherical azimuthal angle $\phi$ of the fiber orientation. (For clarity, only the first quadrant is shown.)

the fibers contained in a volume element $dV$ centered on the point $\mathbf{r}$ are pointing preferentially toward the $\hat{\mathbf{z}}$ axis, more precisely $0 \leqslant \theta < 55°$, or near a plane perpendicular to $\hat{\mathbf{z}}$, where $55° < \theta < 125°$. Within one of those two regions, the magnitude of $\mathcal{S}$ then defines two values of the polar angle: $\theta$ and $\pi - \theta$.

Fig. 4C is a plot of the angular dependence of the total $x$, $y$, and $z$ gradient signals for the square array of four fibers at a correlation distance of 12 grid pts, i.e., three times the correlation distance of Fig. 4B. While the signal amplitudes are generally at least 25% lower than in Fig. 4B, due to spins inside the fibers attempting (unsuccessfully) to couple to spins located in the surrounding (void) space, the angular dependence is much more pronounced than in Fig. 4B. This large difference is likely due to the long-range magnetic interactions between neighboring fibers [27].

A remarkable observation is the extent to which the angular dependence of the subtraction $\mathcal{S} = \|G_Z\| - \|G_Y\| - \|G_X\|$ (Fig. 4F) preserves its functional similarity to that of Figs. 4D and E. This outlines the robustness of the method to changes in fiber density and correlation gradient wavelength relative to the fiber radius. The differences are mainly reflected in an overall scaling factor. The graphs in Figs. 4D–F can be inverted to provide the mapping $g^{-1}$ discussed in Section 1.

Having determined the polar angle $\theta$, we now search for similar relationships defining the azimuthal angle $\phi$. In Fig. 5 are plots of the CRAZED signal intensity for $x$, $y$, and $z$ gradients as function of $\phi$, where $\phi$ is the fiber orientation in the $xy$ plane as measured from the $y$ axis. Calculations are for an array of four parallel fibers (length 35 pts, radius 10 pts) whose principal axes are parallel to the $xy$ plane ($\theta = \pi/2$). Three correlation distances are shown: Fig. 5A is for $d_c = 4$ pts, Fig. 5B is for $d_c = 10$ pts, and Fig. 5C is for $d_c = 16$ pts. At short correlation distance all three curves are nearly identical in shape, however, as $d_c$ increases, the $x$ and $y$ gradient curves depart from each other with the $x$ gradient curve shifting toward the $x$ axis and the $y$ gradient curve, toward the $y$ axis. Thus, there is a clear sensitivity of the $x$ and $y$ gradients to the orientation of fibers in the $xy$ plane.

Since the $x$ gradient curve is strongest when the fiber points along $x$ and likewise for the $y$ gradient curve, it makes sense to look at the subtraction $\|G_X\| - \|G_Y\|$. We define the following ratios:

$$\begin{aligned} \mathrm{GXR} &= \frac{\|G_X\|}{(\|G_X\| + \|G_Y\| + \|G_Z\|)/4}, \\ \mathrm{GYR} &= \frac{\|G_Y\|}{(\|G_X\| + \|G_Y\| + \|G_Z\|)/4}, \end{aligned} \tag{1}$$

which are simply $\|G_X\|$ and $\|G_Y\|$ normalized to the total signal. When determining $\theta$ and $\phi$, it is preferable to normalize to the total signal because the total magnetization density within a volume of interest can change as the fibers are rotated. For example, an infinitely long fiber crossing a cubic volume element will constitute a stronger perturbation of the background magnetization if it is oriented along one of the diagonals, where it occupies a larger volume fraction of the cube.

In Fig. 6, we plot the ratios $GXR$ and $GYR$ as well as their difference $GXR - GYR$, as a function of the azimuthal angle $\phi$ of the fibers in the $xy$ plane. The subtraction leaves two distinct regions, a positive and a negative one which, unlike the $3\cos^2\theta - 1$ dependence, exhibit the same amplitude (i.e., the dependence is more like $2\cos^2\phi - 1$). From this, we conclude that there exists a mapping between $\phi$ and $GXR - GYR$. This graph can be inverted to obtain the mapping $h^{-1}$ mentioned in Section 1. Angles between 30° and 60° are more ambiguously defined than angles near 0° or 90°.

### 2.2. Experimental detection of anisotropy

High resolution magnetic resonance images from the CRAZED sequence with $x$, $y$, and $z$ correlation gradients are shown in Fig. 7. We denote the intensity (magnitude of the complex signal) of the image points by matrix elements $\|G_X\|_{ij}$, $\|G_Y\|_{ij}$, and $\|G_Z\|_{ij}$, respectively. The point-by-point subtraction of the three images, $\|G_X\|_{ij} + \|G_Y\|_{ij} - \|G_Z\|_{ij}$ clearly depicts the phloem region and collenchyma vessels. Some of the tube and celery edges are slightly highlighted; both structures are also anisotropic in their NMR properties. The regions which are highlighted by the subtraction correspond to known vascular structures which exhibit anisotropy along the direction parallel to the slice thickness.

In Fig. 2, there is the inner concave wall of the larger celery stick which appears with a much larger longitudinal equilibrium magnetization than the other walls. This same wall is also highlighted by the subtraction (Fig. 7), as would be expected since the wall provides an anisotropic structure (a surface oriented along the direction of the imaging slice). Other celery walls of smaller longitudinal equilibrium magnetization are not highlighted by the subtraction. Although many different celery specimens were used in this study to ensure repeatability, the specimen shown in Fig. 2 is the same as that of Figs. 7 and 8.

Fig. 8 shows subtraction experiments $\|G_X\|_{ij} + \|G_Y\|_{ij} - \|G_Z\|_{ij}$ but for different values of the correlation distance: 40, 118, 197, and 296 μm. At $d_c = 40$ μm the $n = 2$ CRAZED signal is the more heavily diffusion weighted signal since the RMS diffusion length $\sqrt{2Dt} \approx 20$ μm over the time period $t = \tau + \mathrm{TEeff} = 6\ \mathrm{ms} + 90\ \mathrm{ms}$ along any given direction is 25% of the helix wavelength $\lambda = 80$ μm. For the remaining correlation distances $d_c = 118$, 197, and 296 μm (Figs. 8B–D), the diffusion length is 8, 5, and 3% of the helix wavelength, respectively, which is well outside the diffusion-weighted regime. (These estimates assume a

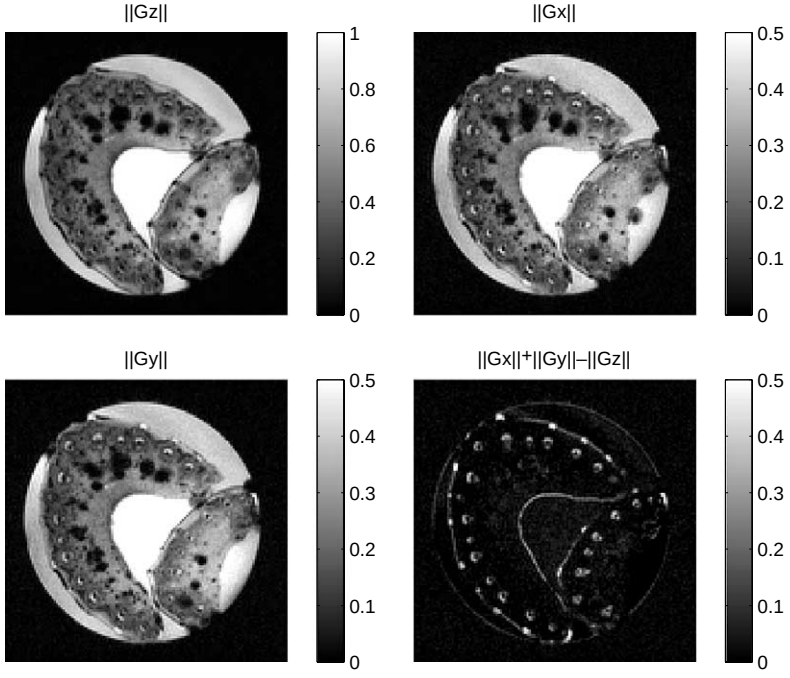


Fig. 7. $n = 2$ CRAZED images with $z$, $y$ and $x$ correlation gradients ($d_c = 180$ μm, $\tau = 36$ ms). The stronger signal intensity of the phloem tissue is evident from the $\|G_X\|$ and $\|G_Y\|$ images. The subtraction $\|G_Y\| + \|G_X\| - \|G_Z\|$ highlights the anisotropic vascular structures (vascular bundles, collenchyma). The maximum observed anisotropy ($\|G_Y\| + \|G_X\| - \|G_Z\|$) is 0.5 in the collenchyma and 0.3 in the vascular bundles.

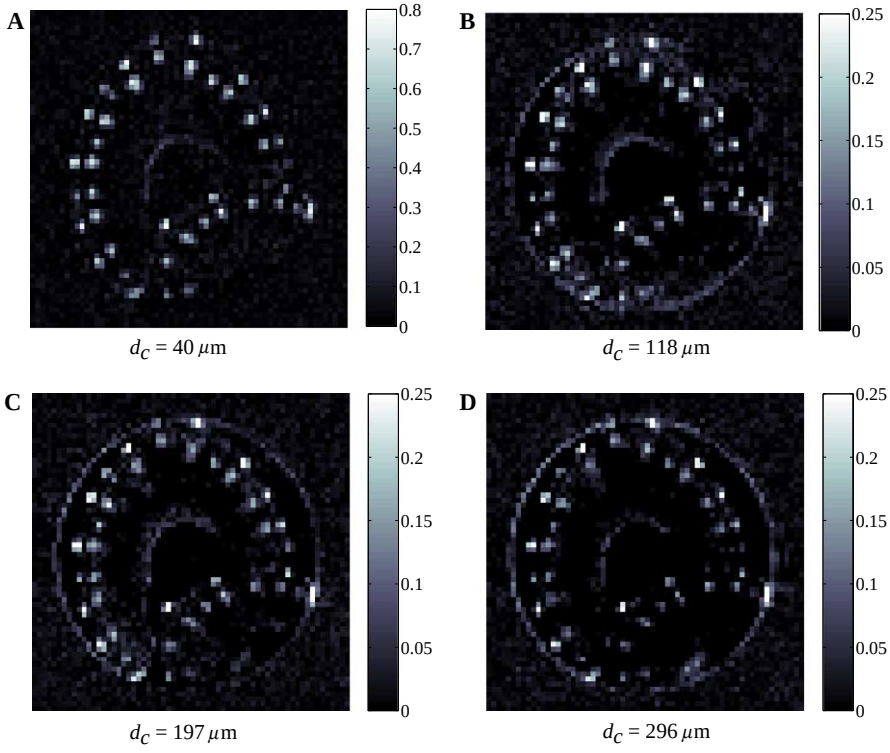


Fig. 8. Subtractions (A–D) $\|G_X\| + \|G_Y\| - \|G_Z\|$ for the case of $\tau = 6$ ms, $d_c = 40$, 118, 197, and 296 μm. Even for weak gradients (B–D) the subtraction clearly highlights anisotropic structures. The maximum observed anisotropy ($\|G_Y\| + \|G_X\| - \|G_Z\|$) in (A) is 0.8 in the collenchyma and vascular bundles. For (B–D) the maximum observed anisotropy is 0.25 in the collenchyma and 0.15 in the vascular bundles. (Images are normalized to the intensity of the water signal (=1.0) in the $G_Z$ image for comparison.)

free diffusion coefficient $D = 2 \times 10^{-5}\,\mathrm{cm}^2/\mathrm{s}$, providing an upper bound for the diffusion length in the restricted environment, while adjusting for the higher effective diffusion coefficient of the double-quantum coherences during the $\tau$ period. See Zhong [28] for details.)

It is also noticeable in Fig. 8A that the diffusion-weighted signal does not highlight the tube edges, but that, for much weaker gradients, the subtraction $\|G_X\|_{ij} + \|G_Y\|_{ij} - \|G_Z\|_{ij}$ is able to detect it. The tube edge detection is stronger at the longest correlation distance, $d_c = 296\ \mu\mathrm{m}$ (Fig. 8D). This further illustrates how the CRAZED signals detect structural anisotropy; a case where there is an absence of magnetization outside the tube, and which does not rely on diffusion effects within confined boundaries.

For comparison, we include conventional pulsed-field gradient [29] diffusion-weighted spin echo images (diffusion delay $\Delta = 20$ ms) in Fig. 9, for two different gradient wavelengths, $\lambda = 40\ \mu\mathrm{m}$ and $\lambda = 80\ \mu\mathrm{m}$. Images shown are analogous subtractions $\|G_X\| + \|G_Y\| - 2\|G_Z\|$, where the factor of 2 is present because for single-quantum coherences (conventional NMR signal) in isotropic media a $z$ gradient signal has the same amplitude as for the $x$ or $y$ gradient; there is no $3\cos^2\theta - 1$ weighting factor, as there is for the truncated dipolar field. Two important differences from the CRAZED subtraction can be seen in these diffusion experiments. First, the tube edges are highlighted in CRAZED but not in the conventional diffusion-weighted image. Second, in the diffusion weighted case, the vascular bundles show the greatest diffusion restriction effects, and therefore appear brighter than any other structure [30]. In the CRAZED subtraction for weak gradients (Figs. 8B–D), on the other hand, it is the collenchyma vessels that appear brightest.

### 2.3. Measurements of vector orientation

The calculations of the previous section are easily verified experimentally by reorienting the celery samples inside the magnet. In a first experiment, the celery is tilted inside the tube by approximately 20° with respect to the applied field. Images of vascular bundle are shown in Fig. 10 for the case of celery aligned along the direction of the applied field, and for the case of a 20° tilt. The image shown is a close-up over a $7 \times 7$ mm region centered on the vascular bundle. The square region centered on the vascular bundle represents a $2.1 \times 2.1 \times 4$ mm volume (the imaging slice is 4 mm thick) over which we integrate the signal to calculate the effects of reorienting

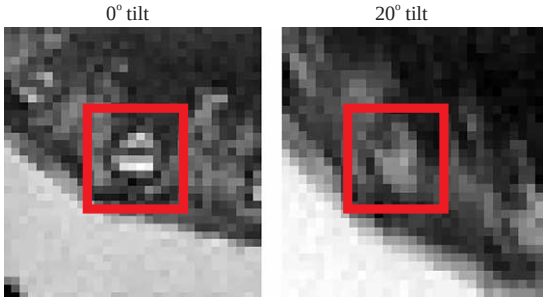


Fig. 10. 7 mm × 7 mm close-up on a vascular bundle showing the effects of a 20° tilt away from the direction of the applied field resulting in reduced signal. The reduced signal makes it possible to resolve the tilt. The square region (2.1 mm × 2.1 mm) delimits the edges of the volume element $V$.

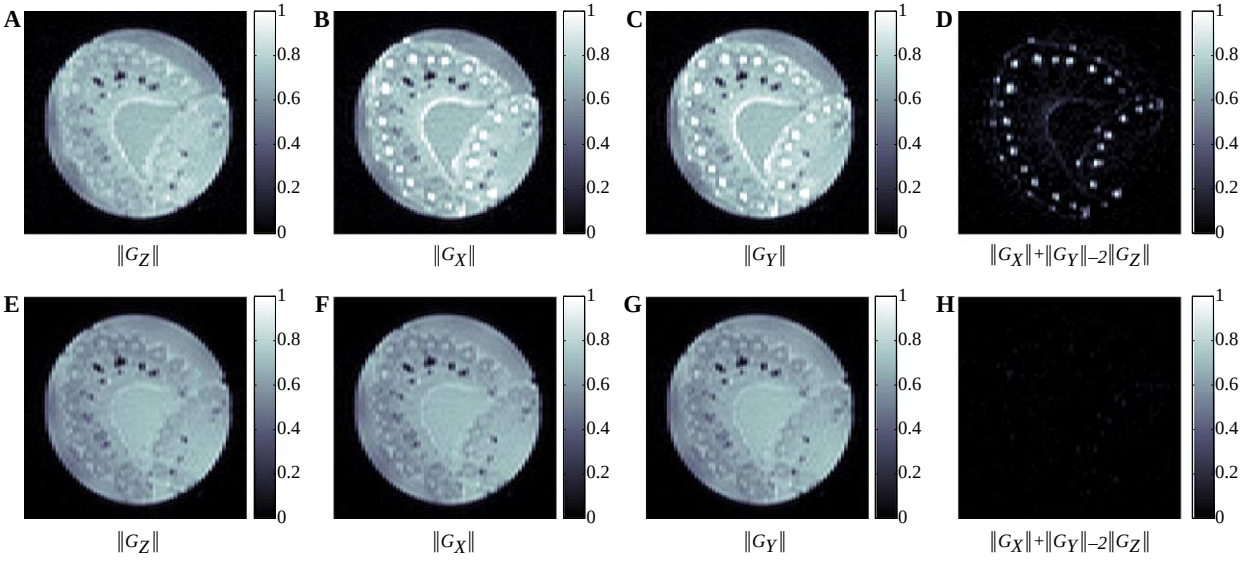


Fig. 9. Subtractions $\|G_X\| + \|G_Y\| - 2\|G_Z\|$ of conventional PFG-SE diffusion weighted images. (A–D) For the helix pitch wavelength $\lambda = 40\ \mu\mathrm{m}$; (E–H) are for $\lambda = 80\ \mu\mathrm{m}$. The $\lambda = 40\ \mu\mathrm{m}$ gradient highlights well the vascular bundles and the collenchyma while the $\lambda = 80\ \mu\mathrm{m}$ gradient is too weak to produce significant diffusion weighting. In (D) the maximum observed anisotropy value is 1.0, while in (H) it is a factor of 12 smaller.

the fibers on the total signal contained in a volume of interest $V$.

While the signal intensity appears lower in the case of the 20° tilt, some of this difference is due to the larger volume fraction the vascular bundles occupy within each voxel as the sample is tilted. This can be corrected for by normalizing the intensity to the total intensity $\|G_X\|_{ij} + \|G_Y\|_{ij} + \|G_Z\|_{ij}$ of each voxel $ij$. A second correction that was done is to normalize both image intensities to the amplitude of the surrounding water, which acts as a reliable reference for the equilibrium magnetization, to compensate for changes in the shimming conditions.

With both corrections applied, we get a 10% decrease in subtraction signal $\sum_{i,j \in V} \|G_Z\|_{ij} - \|G_X\|_{ij} - \|G_Y\|_{ij}$ contained in the volume $V$. Referring to the subtraction curves of Fig. 4A, a 10% decrease in the negative subtraction signal from $\theta = 0$ gives an angle $\theta$ of approximately $15 \pm 5°$, which is reasonably close to 20°. Additional experiments in which the tilted celery was rotated in the $xy$ plane with the azimuthal angle $\phi$ aligned approximately along the lines $\phi = 0°$, 45°, and 90° gave subtractions $GXR - GYR$ which lie within 10% of the calculation results of Fig. 6, including the correct sign (except for the case $\phi = 45°$, for which the sign is ambiguous). The measured GXR and GYR ratios typically overshoot the calculated values by 20%.

## 3. Discussion

### 3.1. Resolution of $\theta$ and $\phi$

Our results suggest a novel method to non-invasively map the fiber orientation in porous materials which exhibit a significant difference in magnetic properties—density or relaxation times—between the fibers and the embedding material. A subtraction $\|G_Z\| - \|G_Y\| - \|G_X\|$ of $z$, $y$, and $x$ gradient images from a CRAZED sequence exhibits a strong angular dependence which allows the resolution of $\theta$, the polar angle of the fiber axis with respect to the applied field. This subtraction is positive near $\theta = \pi/2$ and negative near $\theta = 0$. A subtraction of $x$ and $y$ gradient signals, $\|G_X\| - \|G_Y\|$, allows the resolution of the azimuthal angle $\phi$.

We have also processed this data as phase-sensitive combinations (e.g., $G_Z + G_Y + G_X$ instead of $\|G_Z\| - \|G_X\| - \|G_Y\|$) and observe the same outcomes. The theoretical predictions are also identical since the CRAZED signal in the limit of short evolution times is entirely in-phase. In some cases, we have found the phase-sensitive method to be less reliable due to non-uniform phase rolls across the image. While these effects can be mitigated with slice shimming, the procedure is tedious and inconvenient.

For an isotropic material such as a homogeneous sphere (Fig. 3) the subtraction gives zero since the $x$, $y$, and $z$ gradients give signal magnitudes in ratio 1:1:2, respectively, due to the angular dependence of the dipole field. In celery, the storage parenchyma tissue exhibits no significant degree of anisotropy [30,31]. Hence, the subtraction experiment also does not detect any edges (Fig. 7), as is the case with the surrounding water, which provides a reference point for comparison. In contrast, the collenchyma and phloem tissues are highly anisotropic, and are clearly distinguished on the point-by-point subtraction map.

The noise content of experimental NMR measurements is naturally associated with a higher uncertainty in the angle determination. Referring to Figs. 5 and 6, we see that the uncertainty is highest for angles $\theta$ and $\phi$ near the diagonal direction because of the zero in the subtraction and is lowest in the 0° and 90° regions. In less favorable conditions, depending on the signal to noise ratio, the method may still be capable of determining the 0° from 90° orientations because of the sign change, and the diagonal direction which gives zero in the subtraction.

### 3.2. Magnetic properties and contrast

The detection of anisotropy should be possible provided one of the fundamental NMR parameters—$T_1$, $T_2$, magnetization density or resonance frequency offset—varies significantly over the scale of the correlation distance so as to produce detectable changes following the CRAZED preparation ($M_{eq}$ can be made $T_1$-weighted by shortening the repetition time TR). Our calculations show that the correlation distance should be selected based on a size comparable to or larger than heterogeneities, which should make it suitable for overcoming the limited spatial resolution in MRI.

Although we were unable to determine the upper limit of the correlation distance (or, equivalently, how small a structure can be resolved given a fixed gradient strength) due to the grid size used in the calculation, our results indicate that correlation distances larger than the fiber diameter can be used. Hence, unlike diffusion-based NMR methods where strong gradients modulate the magnetization on the scale of the RMS diffusion length, this method works in a regime independent of diffusion; the gradient strength depends only on the size of material heterogeneities. The gradients can be weak or strong, but generally much weaker than in diffusion experiments.

In the case of celery, the strong contrasts highlighted in the subtraction $\|G_Z\| - \|G_X\| - \|G_Y\|$ in the vascular bundles and collenchyma are likely due to the relaxation times. $T_1$ is 700–1000 ms over the bundles and 2 s in the surrounding parenchyma while $T_2$ is 60–80 ms in the bundles, 110–170 ms in the rim immediately outside and 90–100 ms in the parenchyma. The lower $T_1$ results in a longitudinal equilibrium magnetization that is

about 60% higher than the surrounding parenchyma (Fig. 2). The relaxation times alter the dipolar field, which is calculated using the magnetization following the pulse sequence preparation, which depends on $T_2$ and the steady-state ($T_1$-weighted) equilibrium longitudinal magnetization $M_{eq}$.

The contribution of resonance frequency offsets—such as magnetic field perturbations arising at interface boundaries of regions with different magnetic susceptibilities—plays no important role in the present study. In separate experiments (not shown) the $2\pi$ pulse of the sequence was replaced by a $\pi$ pulse to refocus the contribution of field inhomogeneities [23] and the results did not differ significantly from the CRAZED results. An interesting application of this directional vector imaging method using the dipolar field is for the detection of tumors, where the susceptibility-induced magnetic field perturbations are large enough to be detected in a CRAZED experiment [5].

### 3.3. Anisotropy of structural heterogeneities

The mere presence of structural heterogeneities is not sufficient to produce a detectable signal in the subtractions $\|G_Z\| - \|G_X\| - \|G_Y\|$ or $GXR - GYR$. For subtraction detection and for detection of changes with orientation, it is necessary for the heterogeneities to exhibit a sufficient degree of anisotropy, as is the case for the vascular bundles, collenchyma or the celery and tube edges (Figs. 7 and 8). The term "sufficient anisotropy" is hard to define precisely, but implies that the structures should alter one of the NMR parameters ($T_1$, $T_2$, local magnetization density or resonance frequency offset) and the geometric arrangement should exhibit modulations in at least one parameter along a preferential direction, over a length scale of the same order of magnitude as the correlation distance or longer. Modulations over shorter lengths will not be measured since they will not affect the gradient-induced magnetization grating. For specific geometries, detailed numerical calculations of the NMR signal for a given set of NMR parameters can be performed [32,23] to determine the amplitude of the signal changes upon rotation of a specific heterogeneity.

Fig. 2 shows additional regions of high equilibrium longitudinal magnetization in the shape of triangular-like regions located between the outer celery wall and the vascular bundles. These are part of the parenchyma and do not exhibit any significant degree of anisotropy when probed by diffusion-based techniques [30]. In fact, the subtraction does not highlight these regions (Figs. 7 and 8), suggesting that the heterogeneities in $M_{eq}$ do not form detectable anisotropic structures.

The presence of air bubbles is problematic only to the extent that they may travel during the course of acquisition. The brightest spot in the subtraction image of Fig. 7 is due to a transient air bubble which was present during acquisition of the $\|G_Z\|_{ij}$ image but not for the $\|G_X\|_{ij}$ or $\|G_Y\|_{ij}$ images. Several additional air bubbles can be seen in the storage parenchyma of $\|G_X\|_{ij}$, $\|G_Y\|_{ij}$, and $\|G_Z\|_{ij}$ images. For practical applications, it may be preferable to acquire $x$, $y$, and $z$ gradients during the innermost loop of an imaging sequence rather than acquiring them as three consecutive images (as we have done) to reduce chances of transient air bubbles giving rise to gross artifacts.

### 3.4. Estimating the contrast

For a given material, we may estimate the expected contrast in a subtraction $\|G_Z\| - \|G_X\| - \|G_Y\|$ provided we know the geometry and magnetization distribution. From Fig. 2 the phloem tissue has a longitudinal equilibrium magnetization of 1.0 compared to the surrounding tissue which has a magnetization of 0.6. For a cylindrical fiber of radius 10 embedded in a $80^3$ matrix, the volume fraction of the cylinder is 5% of the embedding matrix. In the subtraction image $\|G_X\| + \|G_Y\| - \|G_Z\|$ of Fig. 7 we find that the subtraction is approximately 0.35 over the phloem. For an embedding matrix of size $80^3$, where this change affects 5% of the volume, this corresponds to 2.5% of the average magnitude of the $\|G_Z\|_{ij}$ image over a similar region. We calculated numerically the subtraction signal $\|G_X\| + \|G_Y\| - \|G_Z\|$ for a fiber of radius 10 pts, pointing along $\hat{\mathbf{z}}$ in an embedding matrix $80^3$ with the same magnetization density distributions (1.0 over cylinder vs. 0.6 outside) and $d_c = 22$ pts. We find that the subtraction signal is 1.5% of the $z$ gradient signal magnitude, which slightly underestimates the experimentally derived value of 2.5%. This estimate is reasonable given that the phloem was approximated by a cylinder.[2]

### 3.5. Applications

The fact that anisotropic structures can be detected with these weak magnetic field gradients outlines the fundamental difference between this technique based on detection of the dipolar field and conventional methods that rely on diffusion or microscopic imaging. The subtraction over the anisotropic vascular bundles results in a fairly strong signal of magnitude comparable to the $\|G_Y\|_{ij}$ or $\|G_X\|_{ij}$ images and to the signal changes observed in diffusion-weighted MRI, despite the weaker gradients used. Thus, the methodology complements currently existing NMR methods by being able to probe intermediate length scales not normally accessible by

[2] A significant source of error is the widely different choices of correlation distance. In the numerical estimate, the wavelength is four times the cylinder radius; whereas the experimental wavelength is below the image resolution (such a short wavelength could not be reproduced in these calculations).

MRI or diffusion-based methods. From the practical standpoint, it may present advantages over DTI to the extent that the reliance on weaker gradients would make it less prone to motion artifacts. Also, only three measurements are required ($x$, $y$, and $z$ gradients) compared to several $b$-values and directions for DTI.

Disadvantages of the method include the ambiguity in the angles $\theta$ and $\phi$ around specific values, and their determination which is not single-valued (i.e. $\theta$ and $\pi - \theta$ are not differentiated). Moreover, care should be taken in ensuring that data from subtraction signals are interpreted under conditions of sufficient signal-to-noise. This is a potential pitfall if the subtractions are normalized to the total signal $\|G_Z\| + \|G_Y\| + \|G_X\|$ within the volume of interest, unless criteria are used to identify regions where the signal-to-noise is too low. Such a discrimination can easily be implemented since the total signal $\|G_Z\| + \|G_Y\| + \|G_X\|$ is readily available from the same data set and requires no additional acquisitions.

The CRAZED signal is approximately 5–10% of the conventional signal, which is usually enough for imaging many materials and tissues. The signal changes upon rotation of the fiber, in our experiments, can reach up to 50% of the CRAZED $\|G_Z\|$ signal (see Fig. 7). For a lone fiber occupying only 10% of the voxel volume, this is about 5% of the CRAZED $\|G_Z\|$ signal, which would be problematic if the conventional signal has signal-to-noise 400:1 or less. In this case, voxel sizes too large should be avoided. For voxels containing bundles of parallel fibers (rather than a lone fiber), this criterion can be relaxed, and this is the regime of operation where the method should be most useful.

Conceptually, since the dipolar field measurements can be averaged over large volume elements, imaging or good spatial resolution is not necessary; it could be used in conjunction with low field systems and for ex-situ NMR/MRI, where measurements are done outside the magnet [33,34]. The much higher immunity of CRAZED measurements to grossly inhomogeneous field environments [23] make it a possible candidate for overcoming some of the challenges associated with imaging in these situations.

This method could be used to probe stratified or lamellar materials whose layers or gaps are on the order of tens of micrometers to millimeters. Such materials, including porous rocks and soils could be probed, provided there is sufficient water content to create a dipolar field for the solution phase. This method is also attractive for tumor imaging, and for tissues known to exhibit anisotropy on the measurable length scales such as trabecular bone [18].

We were able to detect subtraction signals $\|G_X\| + \|G_Y\| - \|G_Z\|$ in fixed rat brain (Fig. 11); the structure is mainly detected in the cortex. This suggests that in vivo measurements should be feasible and possibly more sensitive than in the present study, given the longer relaxation times of live tissue; flow would also introduce further anisotropy effects.

It is instructive to analyze average image intensities over regions of interest and compare the subtraction contrast in rat brain (Fig. 11) to that of celery (Fig. 7). In the $\|G_Z\|$ CRAZED image of Fig. 7, the average signal in the most hydrated regions of the parenchyma reaches up to 90% of the average surrounding water signal whereas the average signal over the brain tissue (Fig. 11) is less than six (6) times that of water. In Fig. 7, the subtraction signal from the collenchyma exceeds half the average signal of the parenchyma, the subtraction signal of the vascular bundles is 1/4 to 1/2 of the parenchyma, while the subtraction signal in the parenchyma (“noise”) is less than 1/10 times the average $\|G_Z\|$ CRAZED signal in the parenchyma. In the rat brain (Fig. 11), the average subtraction signal measured in the region near the tube center reaches nearly 1/4 times the average $\|G_Z\|$ CRAZED signal of the brain, which is

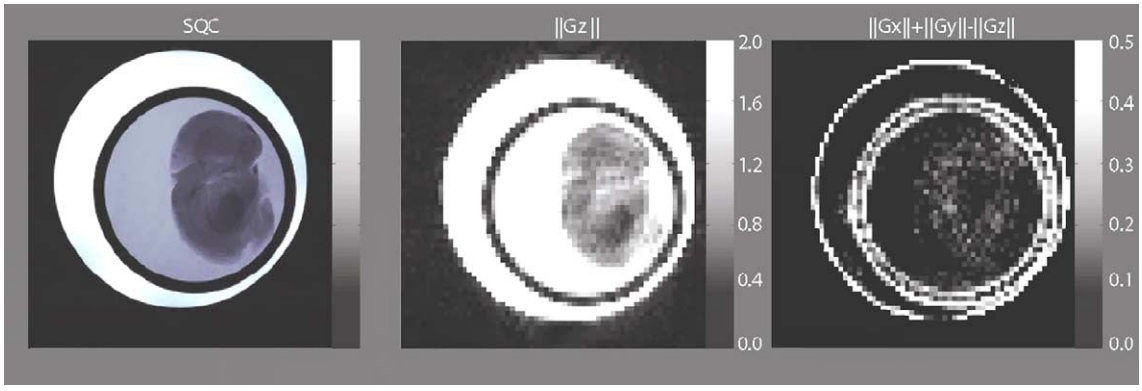


Fig. 11. Multiple-quantum vector imaging in the rat brain. Conventional single-quantum coherence (SQC) spin echo image (left) with TR = 2 s, TE = 74 ms, $n = 2$ CRAZED image ($\|G_Z\|$) with $z$ gradient (center) and anisotropy image (raw subtraction $\|G_X\| + \|G_Y\| - \|G_Z\|$) highlighting various regions of the rat cerebral cortex (right). The rat brain sample was put in a glass tube filled with formalin, and this tube is contained in a larger glass tube filled with water. It is noteworthy that the CRAZED anisotropy image readily highlights the glass tube edges, illustrating the fundamentally different image contrast over SQC. CRAZED parameters were: $\tau = 6$ ms, TEeff = 74 ms, $d_c = 237$ μm, TR = 3 s.

well above the "noise" level in the celery experiments. Finally, we note that the subtraction contrast in Fig. 11 is much stronger at the glass walls than in the brain, mostly likely because the walls are highly anisotropic compared to the brain tissue, whose structure is more random.

A further complication in the analysis of such data is the contribution of image noise to the ambiguity in determining both angles. Such errors could be measured in phantom materials, but its assessment in animal tissue is not trivial due to the randomness of the medium. A detailed study of the contrast effects in animal tissue, including proper histology, microscopy and spatial correlation, is beyond the scope of this research.

We stress the strong likelihood, in this context, that subtraction signals $\|G_X\| + \|G_Y\| - \|G_Z\|$ could also highlight anisotropies in the local resonance frequency. Magnetic susceptibility effects are beyond the scope of this article, but could easily be investigated using the methods proposed herein and numerical calculations that include resonance frequency offsets as we presented in [18]. Another potential application is for prostate cancer, where the parallel vessels in prostate tissue can reach hundreds of micrometers in diameter, and we envisage that anisotropy effects could be detected with this technique.

## 4. Conclusion

In this article, we presented theoretical and experimental evidence towards the development of a non-invasive methodology which uses the dipolar field of a heterogeneous material to map the fiber or vessel orientation. Three NMR images are acquired whose signal is proportional to the dipolar field of the solution phase when the magnetization is modulated sinusoidally along three orthogonal axes. A subtraction $\|G_X\| + \|G_Y\| - \|G_Z\|$ in anisotropic media yields the polar angle $\theta$ of the fiber orientation with respect to the static field, while $\|G_X\| - \|G_Y\|$ gives the azimuthal angle $\phi$.

The magnetic dipole field has the advantage of probing length scales in the range of tens of micrometers to millimeters, which are currently difficult to measure by conventional NMR methods. The major advantage of the method is its reliance on volume-averaged measurements and, therefore, works in cases of poor spatial resolution, where MRI is unable to resolve the individual fibers, or in the case of NMR bulk or voxel measurements. We anticipate this method could be useful in the materials sciences and biomedical imaging, for example, in tumor detection or evaluation of prostate cancer.

## Acknowledgments

This work was funded by NIH Grant EB2122. L.-S.B. gratefully acknowledges financial support from Princeton University through a fellowship. We thank Silvia Cenzano and Marlene Richter for providing the rat brain samples.

## Appendix A

Since the dipolar field is a linear functional of the magnetization, i.e., $\vec{B}[a\vec{M}_1 + b\vec{M}_2](\mathbf{r}) = a\vec{B}[\vec{M}_1](\mathbf{r}) + b\vec{B}[\vec{M}_2](\mathbf{r})$, we decompose the medium as $\vec{M} + \delta\vec{M}$, where $\vec{M}$ is the background magnetization of the embedding matrix and $\delta\vec{M}$ is the "perturbation" in the background magnetization caused by inhomogeneities. The dipolar field then decomposes as $\vec{B} + \delta\vec{B}$, where $\vec{B} = \vec{B}[\vec{M}]$ and $\delta\vec{B} = \vec{B}[\delta\vec{M}]$. For media with small volume fraction perturbations, we have that $\|\delta\vec{M}\|$ is small compared to $\|\vec{M}\| = \int_\Omega |\vec{M}(\mathbf{r})|\,\mathrm{d}^3\mathbf{r}$. Thus, the approximation $\vec{S}[\vec{M}+\delta\vec{M},\vec{B}] \approx \vec{S}[\vec{M},\vec{B}]$ holds in the limit of small $\|\delta\vec{M}\|$, i.e., $\vec{S}[\delta\vec{M},\vec{B}] \ll \vec{S}[\vec{M},\vec{B}]$, where, according to the equation for total signal, $\vec{S}[\vec{M},\vec{B}] \propto \int(\vec{M}\times\vec{B})(\mathbf{r})\,\mathrm{d}^3\mathbf{r}$. Similarly, if $\|\delta\vec{B}\|$ is small compared to $\|\vec{B}\|$, then $\vec{S}[\vec{M},\vec{B}+\delta\vec{B}] \approx \vec{S}[\vec{M},\vec{B}]$ holds.

If $\delta\vec{M}$ is the perturbation of a lone fiber, giving rise to a dipolar field $\delta\vec{B}$, and $\vec{M}$ is the embedding matrix with dipolar field $\vec{B}$, the phase-inverted configuration is the magnetization $\vec{M} - \delta\vec{M}$ with dipolar field $\vec{B} - \delta\vec{B}$. For the single fiber the total signal functional is $\vec{S}[\delta\vec{M},\delta\vec{B}]$. For the phase-inverted configuration, the approximation $\vec{S}[\vec{M}-\delta\vec{M},\vec{B}-\delta\vec{B}] = \vec{S}[\vec{M},\vec{B}] - \vec{S}[\delta\vec{M},\vec{B}] - \vec{S}[\vec{M},\delta\vec{B}] + \vec{S}[\delta\vec{M},\delta\vec{B}] \approx \vec{S}[\vec{M},\vec{B}] + \vec{S}[\delta\vec{M},\delta\vec{B}]$ holds (for arbitrary geometries we have no general way of estimating the size of $\vec{S}[\delta\vec{M},\delta\vec{B}]$ compared to the other terms). Since $\vec{S}[\vec{M},\vec{B}]$ remains invariant during rotation of the fiber, the changes in signal intensities for the single fiber and its phase inverted configuration would be determined by the term $\vec{S}[\delta\vec{M},\delta\vec{B}]$, which characterizes perturbation effects. (Note that if instead of the phase-inverted configuration $\vec{M} - \delta\vec{M}$ we had a perturbation with positive sign $\vec{M} + \delta\vec{M}$, the above approximation applied to $\vec{S}[\vec{M}+\delta\vec{M},\vec{B}+\delta\vec{B}]$ would give the same result.) Thus, we can obtain first order estimates of signal changes with sample rotation even if the background magnetization is subtracted. This approximation is expected to break down at large volume fractions.

Although this approximation cannot be justified rigorously unless $\delta\vec{M}$ and $\vec{M}$ are known, we have tested it numerically, for simple geometries, by comparing to calculations that included various levels of background magnetization. Aside from the total signal being widely different, the relative changes in total signal upon rotation of the fiber are similar in magnitude. The inclusion of background magnetization generally leads to large fluctuations in the total signal with rotation of the fiber arising from incomplete gradient-induced modulations of the magnetization across at the edges

of the sample. In previous studies involving numerical calculations on a discrete grid, such problems were circumvented by choosing an integral number of magnetization helix cycles across the embedding matrix [23,13]; when the sample is rotated in small steps, this leads to artifacts in the numerical calculation. For illustrative purposes, it is sufficient to consider the effects of the perturbation $\vec{S}[\delta\vec{M}, \delta\vec{B}]$ alone.

## References


[1] P. Basser, J. Mattiello, D. LeBihan, MR diffusion tensor spectroscopy and imaging, Biophys. J. 66 (1994) 259–267.

[2] T. Conturo, N. Lon, T. Cull, E. Akbudak, A. Snyder, J. Shimony, R. McKinstry, H. Burton, M. Raichle, Tracking neuronal fiber pathways in the living human brain, Proc. Natl. Acad. Sci. USA 96 (1999) 10422–10427.

[3] L. Bouchard, W. Warren, Reconstruction of porous material geometry by stochastic optimization based on NMR measurements of the dipolar field, J. Magn. Reson. 170 (2004) 299–309.

[4] W. Warren, W. Richter, A. Hamilton Andreotti, B. Farmer, Generation of impossible cross-peaks between bulk water and biomolecules in solution NMR, Science 262 (1993) 2005–2009.

[5] W. Warren, S. Ahn, M. Mescher, M. Garwood, K. Ugurbil, W. Richter, R. Rizi, J. Hopkins, J. Leigh, MR imaging contrast enhancement based on intermolecular zero quantum coherences, Science 281 (1998) 247–252.

[6] J. Waterton, R. Jones, G. Morris, A spatial editing of NMR spectra by use of heteronuclear multiple spin echoes, J. Magn. Reson. 97 (1992) 218–221.

[7] S. Vathyam, S. Lee, W. Warren, Homogeneous NMR spectra in inhomogeneous fields, Science 272 (1996) 92–96.

[8] M. Levitt, Demagnetization field effects in two-dimensional solution NMR, Concepts Magn. Reson. 8 (1996) 77–103.

[9] R. Bowtell, P. Robyr, Structural investigations with the dipolar demagnetizing field in solution NMR, Phys. Rev. Lett. 76 (1996) 4971–4974.

[10] C. Ramanathan, R. Bowtell, NMR imaging and structure measurements using the long-range dipolar field in liquids, Phys. Rev. E 66 (2002) 041201.

[11] R. Bowtell, S. Gutteridge, C. Ramanathan, Imaging the long-range dipolar field in structured liquid state samples, J. Magn. Reson. 150 (2001) 147–155.

[12] P. Robyr, R. Bowtell, Measuring patterson functions of inhomogeneous liquids using the nuclear dipolar field, J. Chem. Phys. 107 (1997) 702–706.

[13] L. Bouchard, R. Rizi, W. Warren, Magnetization structure contrast based on intermolecular multiple-quantum coherences, Magn. Reson. Med. 48 (2002) 973–979.

[14] L. Bouchard, H. Poptani, R. Rizi, J. Glickson, W. Warren, Intermolecular multiple-quantum coherence imaging of murine tumors depends on choice of dipolar correlation distance, in: Proceedings 11th Annual Meeting, International Society for Magnetic Resonance in Medicine, Toronto, 2003, p. 1112.

[15] W. Richter, M. Richter, W. Warren, H. Merkle, P. Andersen, G. Adriany, K. Ugurbil, Functional magnetic resonance imaging using intermolecular multiple-quantum coherences, Magn. Reson. Imaging 18 (2000) 489–494.

[16] J. Zhong, E. Kwok, Z. Chen, FMRI of auditory stimulation with intermolecular double-quantum coherences (iDQCs) at 1.5 T, Magn. Reson. Med. 45 (2001) 356–364.

[17] A. Schäfer, T. Jochimsen, H. Möller, Functional magnetic resonance imaging with intermolecular double-quantum coherences at 3 T, Magn. Reson. Med. 53 (2005) 1402–1408.

[18] L. Bouchard, F. Wehrli, C. Chin, W. Warren, Structural anisotropy and internal magnetic fields in trabecular bone: coupling solution and solid dipolar interactions, J. Magn. Reson. 176 (2005) 27–36.

[19] C. Chin, X. Tang, L. Bouchard, W. Warren, F. Wehrli, Isolating quantum coherences in structural imaging using intermolecular double-quantum coherence MRI, J. Magn. Reson. 165 (2003) 309–314.

[20] S. Brown, P. Sen, D. Cory, Scaling laws in nmr scattering via dipolar fields, J. Magn. Reson. 154 (2002) 154–156.

[21] S. Brown, P. Sen, D. Cory, Nuclear magnetic resonance scattering across interfaces via the dipolar demagnetizing field, J. Chem. Phys. 116 (2002) 295–301.

[22] S. Lee, W. Richter, S. Vathyam, W. Warren, Quantum treatment of the effects of dipole–dipole interactions in liquid nuclear magnetic resonance, J. Chem. Phys. 105 (1996) 874–900.

[23] S. Garrett-Roe, W. Warren, Numerical studies of intermolecular multiple quantum coherences: high-resolution NMR in inhomogeneous fields and contrast enhancement in MRI, J. Magn. Reson. 146 (2000) 1–13.

[24] C. Ramanathan, R. Bowtell, Dynamics of the nuclear magnetic resonance COSY-revamped by asymmetric z-gradients (CRAZED) experiment, J. Chem. Phys. 114 (2001) 10854–10859.

[25] L. Bouchard, Characterization of material microstructure using intermolecular multiple-quantum coherences, Ph.D. thesis, Princeton University (2005).

[26] G. Deville, M. Bernier, J. Delrieux, NMR multiple echoes observed in solid He-3, Phys. Rev. B 19 (1979) 5666–5688.

[27] X. Tang, C. Chin, L. Bouchard, F. Wehrli, W. Warren, Observing Bragg-like diffraction via multiple coupled nuclear spins, Phys. Lett. A 326 (2004) 114–125.

[28] J. Zhong, Z. Chen, E. Kwok, S. Kennedy, Enhanced sensitivity to molecular diffusion with intermolecular double-quantum coherences: implications and potential applications, Magn. Reson. Imaging 19 (2001) 33–39.

[29] P. Callaghan, Principles of nuclear magnetic resonance microscopy, Oxford/Clarendon Press, New York, 1991.

[30] C. Beaulieu, The basis of anisotropic water diffusion in the nervous system—a technical review, NMR Biomed. 15 (2002) 435–455.

[31] F. Vilaine, J. Palauqui, J. Amselem, C. Kusiak, R. Lemoise, S. Dinant, Towards deciphering phloem: a transcriptome analysis of the phloem of apium graveolens, The Plant J. 36 (2003) 67–81.

[32] T. Enss, S. Ahn, W. Warren, Visualization of the dipolar field in solution NMR and MR imaging: three-dimensional structure simulations, Chem. Phys. Lett. 305 (1999) 101–108.

[33] V. Demas, D. Sakellariou, C. Meriles, S. Han, J. Reimer, A. Pines, Three-dimensional phase-encoded chemical shift MRI in the presence of inhomogeneous fields, Proc. Natl. Acad. Sci. USA 101 (2004) 8845–8847.

[34] C. Meriles, D. Sakellariou, H. Heise, A. Moulé, A. Pines, Approach to high-resolution ex situ NMR spectroscopy, Science 293 (2002) 82–85.